remote sensing

MDPI

Article

Dynamics of the Estuarine Turbidity Maximum Zone from Landsat-8 Data: The Case of the Maroni River Estuary, French Guiana

Noelia Abascal-Zorrilla [1,*], Vincent Vantrepotte [2], Nicolas Huybrechts [3,4], Dat Dinh Ngoc [5], Edward J. Anthony [1,6] and Antoine Gardel [1]

1 Centre National de la Recherche Scientifique-CNRS, UG, IFREMER (LEEISA URS 3456), Centre de Recherche de Montabo, 97334 Cayenne, French Guiana; anthony@cerege.fr (E.J.A.); antoine.gardel@cnrs.fr (A.G.)
2 Laboratoire d'Océanologie et de Géosciences, Université du Littoral-Côte-d'Opale, CNRS, Université de Lille, 32 Avenue Foch, 62930 Wimereux, France; vincent.vantrepotte@univ-littoral.fr
3 Cerema, HA Research Team, 134 rue de Beauvais, 60280 Margny-lès-Compiègne, France; nicolas.huybrechts@cerema.fr
4 Sorbonne Université, Laboratoire Roberval—FRE UTC—CNRS 2012, Université de Technologie de Compiègne, Centre de Recherche de Royallieu CS 60319, 60203 Compiègne, France
5 Space Technology Institute, Vietnam Academy of Science and Technology, 18 Hoang Quoc Viet, Cau Giay, Hanoi 100000, Vietnam; dndat@sti.vast.vn
6 Aix Marseille University, CNRS, IRD, INRA, Coll France, CEREGE UM 34, 13545 Aix-en-Provence, France
* Correspondence: noelia.abascal-zorrilla@etu.univ-guyane.fr

Received: 8 May 2020; Accepted: 3 July 2020; Published: 7 July 2020

Abstract: The estuarine turbidity maximum (ETM) zone occurs in river estuaries due to the effects of tidal dynamics, density-driven residual circulation and deposition/erosion of fine sediments. Even though tropical river estuaries contribute proportionally more to the sediment supply of coastal areas, the ETM in them has been hardly studied. In this study, surface suspended particulate matter (SPM) determined from OLI (Operational Land Imager)-Landsat 8images was used to gain a better understanding of the spatio-temporal dynamics of the ETM of the tropical Maroni estuary (located on the Guianas coast, South America). A method to estimate the remotely-sensed ETM location and its spatiotemporal evolution between 2013 and 2019 was developed. Each ETM was defined from an envelope of normalized SPM values > 0.6 calculated from images of the estuary. The results show the influence of the well-marked seasonal river discharge and of tides, especially during the dry season. The ETM is located in the middle estuary during low river-flow conditions, whereas it shifts towards the mouth during high river flow. Neap–spring tidal cycles result in a push of the ETM closer to the mouth under spring-tide conditions or even outside the mouth during the rainy season. An increase in SPM, especially since 2017, coincident with an extension of the ETM, is shown to reflect the periodic influence of mud banks originating from the mouth of the Amazon and migrating along the coast towards the Orinoco (Venezuela). These results demonstrate the advantages of ocean color data in an exploratory study of the spatio-temporal dynamics of the ETM of a tropical estuary, such as that of the Maroni.

Keywords: estuarine turbidity maximum; Landsat-8; tropical estuary; mud banks; French Guiana

1. Introduction

The trapping of suspended particles in river estuaries can often lead to the formation of highly turbid concentrations, sometimes culminating in the generation of an estuarine turbidity maximum (ETM). The ETM commonly occurs near the upstream limits of the salinity intrusion and can be the result

of the combined effects of density-driven residual circulation, tidal dynamics and erosion and deposition of fine sediments [1]. The ETM plays an important role in biological productivity and sedimentary processes and can be a significant source of fine-grained sediment supply within and outside the confines of estuaries [2–4]. Tropical rivers, located in areas of the world with high chemical weathering rates, between 30°N and 30°S, have been considered as contributing proportionally more fine-grained sediment to their estuaries than mid-latitude rivers [5]. Such tropical estuaries are commonly bordered by mangroves that trap sediments [6–9] and affect flushing rates [10,11], thus contributing to the dynamics of the ETM. Unfortunately, studies dealing with the ETM in tropical estuaries are relatively scarce when compared to those devoted to the study of estuarine hydrodynamics [12–16].

In exceptional circumstances, tropical estuaries can be influenced by lateral mud dispersal systems driven by wind-, wave- or tide-induced currents. Lateral mud dispersal is associated with a number of deltaic systems such as the Jaba and Purari in Indonesia [17] and the Ayeyarwady, the mud supply of which penetrates into the Sittang River estuary in Myanmar [18]. This can also occur where a series of estuaries are affected by an alongshore mud belt such as along the coast of West Africa between Sierra Leone and Guinea-Bissau [19]. The world's largest mud-dispersal system is situated on the north coast of South America (the Guianas coast) between the mouths of the Amazon and Orinoco Rivers. The equatorial Guianas coast is under the influence of muddy deposits supplied by the Amazon River, estimated as ranging from 754 to 1000 million tonnes a year [20,21]. Mud migrates alongshore in a well-defined belt comprising at any time 15–22 mud banks between the zone of mud-bank formation (Figure 1a) and the Orinoco River (Venezuela). Mud banks exhibit extremely high mud concentrations [22]; each mud bank can be up to 5 m thick, 10–60 km long and 20–30 km wide and may contain several times the annual mud supply of the Amazon [23]. These large mud banks migrate along the coast under the influence of wind-generated waves and currents [24–28] at a mean velocity of about 2.3 km/year [29]. A bank migrating alongshore is separated from its neighbors along the coast by inter-bank areas where, in the absence of mud-bank-induced dissipation of wave energy, coastal erosion prevails. Since the banks migrate alongshore, the shoreline at any point will swing over time between bank (accretion) and inter-bank (erosion) phases. Accretion phases are associated with the accumulation of mud and onshore welding of mud banks along the coast. These processes are of biological importance, as they are associated with rapid and large-scale mangrove colonization, creating an ecotope for fish and shrimp development, but they also affect human activities such as access to river ports and maritime traffic and access to beaches. During such phases, mud banks also provide an important external source of sediments, which, under the combined effect of tidal currents and trade-wind waves, can be resuspended and intrude into the numerous estuaries [14] lining the humid tropical coasts of the Guianas. The ETM can, thus, be significantly modified during these phases by the presence of mud banks, with navigation channels behaving as mud traps [30]. However, very little is known of the influence of mud-bank migration on the ETM in the Guianas estuaries and how the ETM evolves in the course of the highly seasonal equatorial rainfall regime.

Two basic types of estuaries have been identified on the Guianas coast [31]. The first type is characteristic of small-catchment rivers with low discharge, resulting in a consequent deflection of the river mouth by a mud cape. The second type is characterized by high river discharge, which slows down mud-bank migration through what has been assimilated by the authors to a "hydraulic-groyne" effect [32] that favors accretion on the updrift coast without the emergence of a cape. To date, several studies have been conducted on the Maroni River, representative of this second type, which was the focus of our study. The previous studies on the Maroni have been devoted to the geochemistry of suspended matter [33,34] and to hydrodynamic controls on sediment distribution patterns, notably at the mouth [15,16,35]. Although the latter studies have highlighted some of the hydrodynamic processes and sediment circuits, including sediment exchanges with the shoreline [36], the seasonal dynamics and processes involved in the ETM in seasonally variable estuaries such as the Maroni, and under the influence of mud banks from the Amazon, are still poorly known. Such studies are, however, an important pre-requisite for river-mouth development projects on this coast.

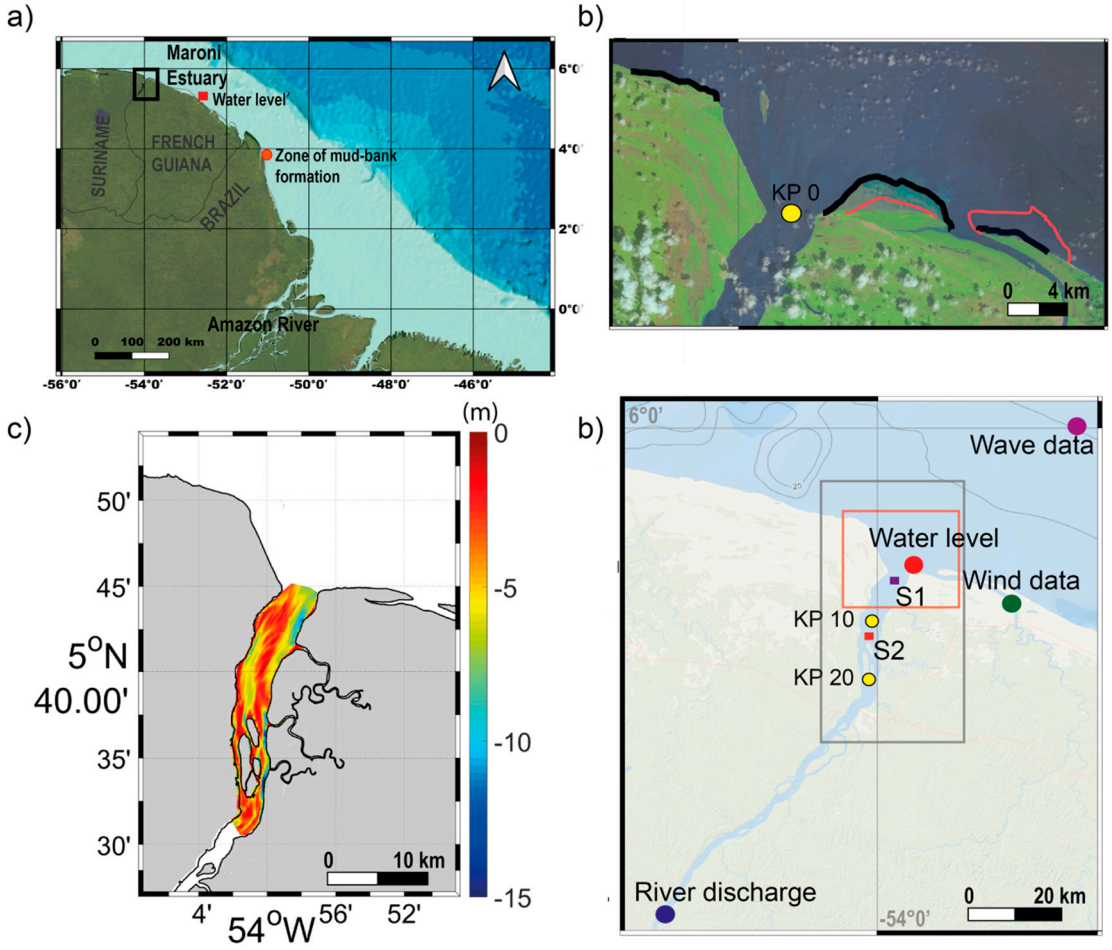

Figure 1. Maroni River and estuary. (**a**) Location of the Maroni River and estuary (black rectangle) in South America, with the red dot north of the mouths of the Amazon showing the area where mud banks formed from the massive mud discharge of this river start migrating westward. The red square shows the location of Île Royale where tide level data were retrieved. (**b**) Mouth of the estuary and limits in 2013 (red line) and 2019 (black line) of the intertidal part of the mud bank that has been present in the Maroni estuary since 2011. The yellow dot shows location of KP 0. (**c**) View of the estuary depicting locations where river discharge (blue dot), wind data (green dot), tide levels (point: Les Hattes, red dot) and wave data (purple dot) were collected. S1 and S2 correspond to the satellite-image areas used to estimate SPM evolution. Location of Kilometric Points (KP) 10 and 20 (yellow dots), which represent distances, in kilometers, along the estuary starting from KP 0. (**d**) Bathymetry of the Maroni estuary from two surveys conducted in 2016 and 2017 [36]. Bathymetry in (**a**) is from GEBCO bathymetry data and in (**c**) from NOAA Bathymetric Data Viewer.

Although the Maroni and several other Guiana estuaries are large estuaries in their own right, the periodic influence of Amazon mud is expected to induce patterns in ETM distribution and dynamics that can be quite challenging to unravel as field approaches systematically entail considerable logistical difficulties [31]. Earth observation methods can overcome to a certain extent the problems of spatial and temporal relevance of in-situ estuarine monitoring, as they can provide a synoptic perspective. Remote sensing data from satellite imagery have, indeed, enabled advances in understanding of the dynamics of the large mud-bank and inter-bank systems [29,37,38]. Recently-launched high-resolution sensors, such as Landsat 8 (16 days of temporal resolution and 15–60 m of spatial resolution) and Sentinel 2 (5 days of temporal resolution and 10–60 m of spatial resolution), present a spatial scale that can improve significantly the study of the small-scale spatial variability of the high inshore mud-concentrations of the Guianas [29]. The estimation of suspended particulate matter (SPM) concentration from ocean

color remote sensing can, therefore, potentially provide relevant information on mud dynamics in estuaries such as the Maroni river.

The objective of this work was to assess the potential of such high-resolution sensor information in contributing to the understanding of the spatio-temporal dynamics of the Maroni estuary under a phase of significant mud-bank influence that has prevailed since 2011 [36]. Due to the complex dynamics that characterize the ETM zone and the challenges of identifying SPM depth concentration gradients, and given the opportunities for the observation of the surface of the water column offered by satellite data, we defined in this study a number of ETM situations from an envelope of normalized SPM values. From this, we propose an exploratory approach that can lay the foundations for more detailed remote sensing-based studies of the ETM. In the frame of this study, SPM variability in the Maroni waters was analyzed from Landsat 8 scenes for the period between April 2013 and June 2019 and confronted with dynamic drivers deemed as important in influencing the ETM. The spatio-temporal evolution of the ETM was evaluated and described based on regional climate seasonality and changes in neap–spring tidal cycles, and the identified patterns are discussed below.

2. Study Area and Methodology

2.1. Maroni River and Estuary

The Maroni River is located in French Guiana, South America (Figure 1), and is subject to a humid tropical-equatorial climate. The region is influenced by seasonal variations caused by the north–south movement of the Intertropical Convergence Zone (ITZC) with a well-marked rainy season from the end of December to July and a dry season from August to December. The rainy season is usually interrupted by a one-month period with dry conditions around March.

The Maroni River is 612 km long and lies astride French Guiana and Suriname (Figure 1a,b), and its mouth lies approximately 700 km northwest of the mouths of the Amazon. Its catchment covers an area of 66,184 km^2, cut in crystalline rocks of the Guiana Shield, and it has a mean water discharge of ~774 m^3/s during the dry season and 2400 m^3/s during the rainy season. Rousseau et al. [34] showed that the Maroni's seasonality index (SI), which is the ratio between the highest monthly discharge divided by the lowest one, is much higher than that of the Amazon, thus highlighting the high seasonality of the freshwater input. This is probably related to the lower dampening effect on water discharge resulting from the much smaller catchment of the Maroni, compared to the Amazon (catchment size of 3.6 million km^2 and mean discharge of 200,000 m^3). Discharge, however, is not erratic in this equatorial setting and increases gradually as the rainy season sets in (see Section 2.3). The Maroni presents a large funnel-shaped shallow estuary mouth rich in sand deposits, indicating the importance of fluvial bedload supply in the system [36].

Tides in the Maroni estuary are semidiurnal and low mesotidal with a range from up to 2.5 m during spring tides [22] to up to 1.1 m during neap tides. The estuary shows a converging plan shape, with tidal range amplification at about 8 km from the mouth [15]. Ross et al. [16] identified an ebb channel at the west bank of the estuary (Suriname) and a flood channel at the east bank (French Guiana) (Figure 1c). A mud bank started impinging on the mouth of the Maroni in 2011 (Figure 1d) [36], and it is still migrating across the estuary.

Onshore-directed northeast trade winds characterize the rainy season, whereas offshore southwest trade winds are dominant when the ITZC is at its northern position during the dry season [27]. The strongest winds in the year occur from January to April [39]. The interaction of the North Brazil Current (NBC), the seasonally variable trade winds and surface gravity waves result in the advection of Amazon mud in a low-salinity plume along the coast to the northwest [40,41]. This migration affects the coastal waters off French Guiana, Suriname, Guyana and Venezuela making this the longest muddy coast in the world.

The salinity intrusion length in the Maroni varies from the dry to the wet season, reaching ~12 and ~5 km upstream from the mouth (corresponding to Kilometric Point (KP) 0; Figure 1d), respectively,

with strong stratification during the rainy season marked by a salty mass of water during high tides [15]. This study also showed a high seasonality in the estuary's turbidity and identified an ETM during the rainy season at the river mouth [15]. Two large tidal creek networks debouch on the river's east bank near the mouth, and a series of shoals and vegetated islands have accumulated between KP 15 and KP 26.5 (Figure 1c). The total suspended solid concentration in French Guiana rivers is low [42], and the Maroni has been identified as among the world's rivers with the lowest concentrations [43], no doubt a reflection of the highly crystalline basement rocks and still largely forested nature of the catchments. However, Gallay et al. [44] identified a notable 239% increase in the Maroni River's SPM after 2009 due to an upsurge in anthropogenic activities, notably gold mining and deforestation.

The Maroni River banks host the twin towns of St. Laurent du Maroni (French Guiana) and Albina (Suriname) about 20 km upstream from the mouth. These are among the fastest growing towns in the Guianas, notably St. Laurent du Maroni, where port facilities capable of handling large ocean-going vessels are being planned, providing a further justification for a better understanding of the mud dynamics at the mouth of the river.

2.2. Satellite Data

2.2.1. Landsat 8 OLI Data Set

Landsat 8 images were used in this study. The Operational Land Imager (OLI) sensor has eight bands at 30 m spatial resolution and a panchromatic one at 15 m spatial resolution. The sensors present four visible bands (1–4), a near infrared band (NIR) and two bands (6 and 7) in the shortwave infrared spectral region (SWIR).

OLI level 1 data (L1T) corresponding to the period between April 2013 and June 2019 were downloaded from the Earth Explorer database (https://earthexplorer.usgs.gov/). In total, 66 Landsat 8-OLI images (Table 1) were used after images highly affected by clouds were discarded.

Table 1. Dates of Landsat 8 images used for the different study years and the two different seasons.

	2013	2014	2015	2016	2017	2018	2019
Rainy season	-14 July -30 July	-14 May -17 July	-09 January -25 January -10 February -17 May -02 June -18 June -04 July	-12 January -16 March -01 April -06 July -22 July	-04 April -20 April -25 July	-01 January -22 March -23 April -12 July -28 July	-20 January -21 February -25 March -26 April -28 May
Dry season	-15 August -31 August -02 October -03 November -19 November -05 December	-18 August -03 September -19 September -05 October -06 November -24 December	-05 August -06 September -22 September -24 October -09 November -11 December	-24 September -10 October -26 October -11 November -27 November -13 December -29 December	-10 August -26 August -27 September -13 October -16 December	-13 August -29 August -14 September -30 September -16 October -01 November -19 December	-

2.2.2. OLI Remote Sensing Reflectance (R_{rs}) Processing

Quasi-permanent glint contamination is present in the study area as a consequence of the characteristics of the OLI sensor, such as the solar viewing path geometry, and the low latitude of the Maroni River and estuary (5°–6°N). This results in the loss of contaminated pixels over the river and estuary. To recover these contaminated pixels, the images were corrected for this effect using the method proposed by Abascal-Zorrilla et al. [45].The method uses SWIR information to perform an automatic correction of this effect based on the assumption that the water-leaving radiance is negligible on this band. For application of a blind correction, several masks have to be defined, such as the land mask, the clear waters mask and the sun glint mask. Once the regions of interest are defined, the SWIR-based empirical approach was deployed following a two-step procedure: the definition of the spectral slope parameter, which allows relating the sun glint observed in the SWIR signal to the

one of the NIR and visible bands to be corrected, and the estimation of the offset value corresponding to the background SWIR 2 of the areas not affected by sun glint.

ACOLITE software (acolite_win 20170718.0), developed at the Royal Belgian Institute of Natural Science (RBINS), was used to process L1T sun glint-corrected images. No external measurements are needed to perform the atmospheric correction using this software. The OLI dataset was processed with the ACOLITE SWIR processing using a fixed epsilon computed on the data prior to sun glint correction, as explained by Abascal-Zorrilla et al. [45]. The ACOLITE atmospheric correction chain used in the framework of this study was validated for French Guiana [45] and R_{rs} data were obtained for the study area.

2.2.3. Post-Treatment of R_{rs} Data

Clouds and Cloud-Shadow Detection

Cloud-shadow detection is one of the limitations of high spatial-resolution sensors. In this study, water pixels (considering the detection of cloud shadows and thin clouds) of the ACOLITE sun glint-corrected images were identified using an algorithm of water-pixel extraction (WiPE) [46]. This algorithm was developed for Landsat 8-OLI and Sentinel 2-MSI and consists of a two-step procedure that considers the statistical analysis of the Rayleigh-corrected top of the atmosphere (TOA) reflectance ($\rho_{rc}(\lambda)$). The first step uses ($\rho_{rc}(\lambda)$) and the spectral shape analysis of each object is performed allowing water pixels to be identified and separated from cloud, vegetation, barren land and construction pixels. The Hue–Saturation–Value space is estimated during the second step, which allows a better detection of cloud shadow over waters and considering the whole image. The two-step algorithm allows the identification of thin clouds and showed a better performance over turbid waters than other algorithms [46].

Estimation of SPM

The estimation of SPM was conducted using a semi-analytical algorithm developed by Han et al. [47]. This algorithm was chosen because it covers four orders of magnitude, from clear to very turbid waters and because it was developed for several sensors, including Landsat 8, and for several water masses, including French Guiana.

SPM estimation was defined using two distinct algorithms related to turbidity levels of the water masses. A smooth procedure was applied to avoid any regularity in the turbidity levels between medium and high turbidity situations. The reader interested in the algorithm is referred to the work of Han et al. [47].

2.2.4. ETM Detection

Based on the different SPM attributes of the images and given that the ETM is affected by different dynamic drivers, its clear identification at the water column surface becomes, in some cases, a difficult task. To overcome this hurdle, a simple methodology was applied to the SPM values (in mg/L, estimated using the algorithm evoked in Section 2.2.3 to identify the presence of the ETM and its dynamics.

1- SPM normalization: The SPM values of each of the scenes in this study were normalized using the values corresponding to the 95th percentile estimated for each of the scenes. This normalization was performed to compare the different maps and to estimate the position of the ETM. The 95th percentile was selected to avoid outliers in the coastal areas, as in French Guiana SPM concentrations in the nearshore area (intertidal part of the mud banks) are characterized by high values [37].

2- SPM-normalized average: SPM-normalized values were averaged over time to estimate the different seasonal and inter-annual conditions. SPM-normalized values were also averaged for different tidal and flow-rate conditions (see figure captions in Section 3 for the number of maps used for the different conditions).

3- Definition of the ETM zone: The limits of the ETM were defined from an envelope of SPM-normalized values higher than 0.6. This > 0.6 threshold value was empirically defined following extensive work using remote sensing data on the muddy coast of the Guianas [29], and it was averaged for the different years and seasonal conditions.
4- Length and core of the ETM zone: The length was estimated to gain insight on ETM spatio-temporal variations. We use the terminology of Uncles et al. [48] to identify a "tail" and a "nose" (which represent, respectively, the downstream and upstream separation of the ETM from areas of lower turbidity). The core of the ETM was estimated from the barycenter using the geometric properties tool in QGIS software.

2.2.5. Data Processing

To identify the relationship between SPM values, on which ETM identification is based, and the influence of different dynamic drivers, a mean SPM value was estimated using the selected scenes without applying the previous normalization step of the methodology (see Sections 3 and 4).

Image classification as a function of the tide (neap, spring or mean) was performed as follows based on the tidal range:

1- Estimate the peak values of the tide series.
2- Estimate the mean and standard deviation values (peak std) of the identified peaks.
3- Tides are defined as follows: Neap tides: $tidal\ values < mean\ peak\ value - \left(\frac{1}{3} peak\ std\right)$ tidal Spring tides: $tidal\ values > mean\ peak\ value + \left(\frac{1}{3} peak\ std\right)$ tidal values>mean peak mean value+((1/3) * peak std). Mean tides: tidal values between those of neap and spring tides.

2.3. Water Levels, River Discharge, Wind and Wave Data

Maroni water discharge data are only available as daily means and were obtained from the database of the service Fleuves, Littoral, Aménagement et Gestion (FLAG) of the DEAL (Direction de l'environnement, de l'aménagement et du logement) (http://hydro.eaufrance.fr/). Data were collected at Apatou (~80 km upstream from KP 0; Figure 1b) between January 2013 and June 2019.

Water levels were retrieved from the tidal gauge record of Les Hattes (5°45′00″N, 53°57′00″W Figure 1b). Due to the short length of the record, which does not cover the entire study period, water level data were also retrieved from the tidal gauge of Île Royale (5°17′06″ N, 52°34′48″ W Figure 1a). The data are managed by the Service Hydrographique et Océanographique de la Marine (SHOM) and Direction de la Mer-Guyane (http://data.shom.fr/). Both series were compared to extract the lag difference between Île Royale and Les Hattes, in order to use the Île Royale data with the lag time corrected.

Wind velocity data (averaged every 10 min) were provided by MeteoFrance at Mana airfield (5°39′48″ N, 53°45′42″ W; Figure 1b) for the period 2015–2019. As our study period starts in April 2013 and the station data start in 2015, wind velocity data were also retrieved from the WAVEWATCH III (WWIII) model [49–51] which is a third-generation wave model developed by NOAA's National Center for Environmental Prediction (NCEP). The data concern the u and v wind components (scaled to a reference height of 10 m). WWIII monthly averaged data (Figure 2c) turned out to be accurate when compared with in-situ data (R^2 = 0.9) (Figure 2c); therefore, these data were used, instead of the station data, for the period 2013–2019. Wave and wind characteristics were extracted from the global model (http://polar.ncep.noaa.gov/waves/) (Figure 1b, wave data) at a spatial resolution of 0.5° × 0.5° and a 3-hourly time resolution from January 2013 to June 2019, corresponding to our study period. Wind in French Guiana blows with mean velocities of 6.3-8.2 m/s and from a north to east-northeast window (Figure 2c,d).

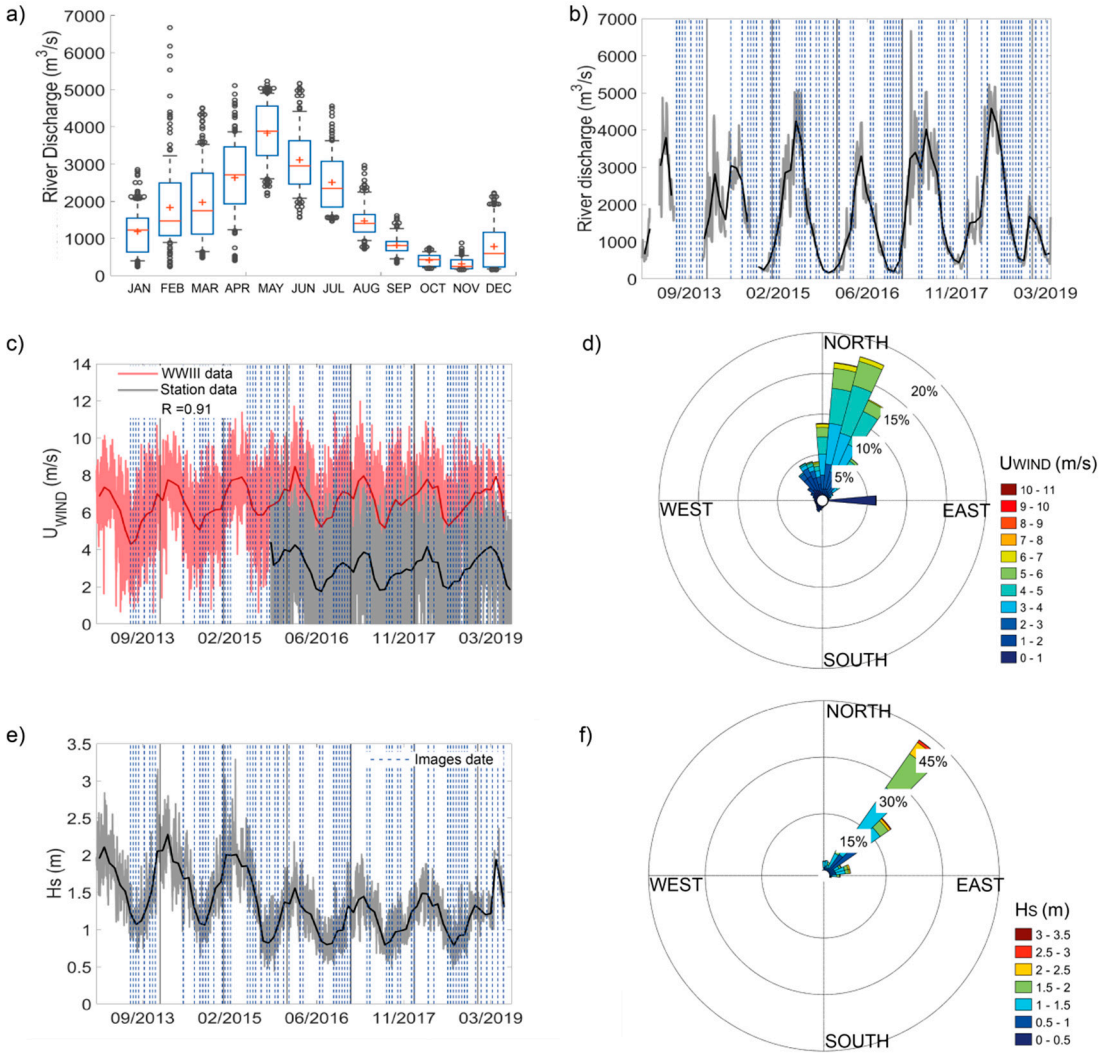

Figure 2. Climatological data. (**a**) Mean annual cycle of monthly river discharge and (**b**) temporal pattern between April 2013 and May 2019. (**a**) Median (red bar), mean (red cross), 25th and 75th percentile values (blue bars) and 9th and 91st percentile values (black lines) of monthly river discharge between 2013 and 2019. (**c**) Temporal pattern of wind velocity data (U_{WIND} (m/s)) and monthly average time series using WWIII data (red lines) and Meteofrance data at Mana airfield station (Figure 1b) (black lines). (**d**) Wind rose for the period 2015–2019 (MeteoFrance data). (**e**) Temporal pattern of significant wave heights (H_s (m)) and monthly average time series using WWIII data (Figure 1b) and (**f**) rose of significant wave heights for the period 2013–2019. The blue lines in (**b**,**c**,**e**) correspond to the dates of the Landsat 8 images used in this study.

Wave data were also retrieved from WWIII for an offshore point where water depth is about 25 m (Figure 1b, wave data), well beyond the zone of coastal mud-bank influence on waves. The model provided significant wind and swell wave heights (m), the primary mean wave periods (s) and the primary wave directions (degrees true, defined as 0° coming from north and 90° coming from east). These variables were monthly-averaged for the study area (Figure 2e). Waves in the Maroni estuary area arrive from an east to northeast direction (Figure 2d,f) in response to the predominant trade winds. High waves prevail between October and May, and smaller waves from June to September (Figure 2e). Significant wave heights have tended to exhibit a decreasing trend since 2015, with maximum values dropping from 2.3 to 1.6 m (Figure 2e).

3. Results and Discussion

In this section, an analysis and discussion of the evolution of the spatial patterns of the ETM, identified using the SPM-envelope methodology defined in Section 2.2.4, is performed as a function of seasonal and interannual conditions. Besides the influence of the tide and the neap–spring cycle in both the dry and the rainy seasons, the way these two seasons affect the ETM is also discussed. Other points of discussion are the influence of river discharge on the ETM and of the presence of the mud bank in the study area since 2011 [36]. Due to the complexity of the dynamics in the study area, the differences in SPM values for the different images and the way they influence detection and extension of the ETM in situations of different dynamic forcing are also important themes that merit discussion in this section. Finally, the question of the frequency of the images in capturing ETM dynamics is also assessed.

3.1. Seasonal and Interannual Spatial Patterns

The seasonal and inter-annual variations of the turbidity of the Maroni estuary are analyzed in terms of spatial differences. Normalized SPM values were estimated as explained in Section 2.2.4 and averaged to calculate the location and extension of the ETM under different conditions (dry and rainy season) (Tables 2 and 3) and years (between 2013 and 2019) (Figure 3). As stated above, the outlines of the ETM have been defined using normalized values above 0.6 for the averaged seasonal and inter-annual situations. Figure 3 depicts a synthesis of the averaged annual and seasonal situations. SPM values are affected by the combined influence of tidal currents, river discharge, winds and waves, such that instant SPM spatial patterns are quite heterogeneous.

Table 2. Extension in km^2 of the ETM for the years between 2013 and 2019 and for the rainy and the dry seasons of each year estimated using ETM delimitation when SPM-averaged values were higher than 0.6.

Extension	2013	2014	2015	2016	2017	2018	2019
Extension total (km^2)	55.2 ± 36.9	57.9 ± 23.7	57.8 ± 13.3	61.9 ± 23.1	52.6 ± 13.0	69.4 ± 19.9	76.6 ± 28.7
Rainy season (km^2)	40.3 ± 13.6	41.8 ± 9.3	54.7 ± 9.5	74.9 ± 21.4	52.1 ± 12.8	68.3 ± 27.1	76.6 ± 28.7
Dry season (km^2)	60.2 ± 27.9	61.9 ± 27.4	49.7 ± 17.5	59.7 ± 22.1	53.1 ± 16.5	69.9 ± 15.5	-

Table 3. Distances of the nose, tail and core of the ETM along the axis of the estuary relative to KP 0 (negative values indicate distances seaward of KP 0) for the years between 2013 and 2019 and for the rainy and the dry seasons of those years.

From KP 0	2013	2014	2015	2016	2017	2018	2019
Tail (km)	4.8 ± 5.5	7.4 ± 6.1	2.4 ± 5.5	2.0 ± 4.1	−0.2 ± 3.9	−2.2 ± 5.7	−1.5 ± 3.4
Tail Rainy	6.1 ± 4.9	2.4 ± 11.6	−0.2 ± 4.1	−1.1 ± 2.5	−3.4 ± 2.9	−3.6 ± 7.7	−1.5 ± 3.4
Tail Dry	4.5 ± 6.0	9.0 ± 3.5	5.5 ± 4.5	4.2 ± 3.4	1.7 ± 6.7	−1.5 ± 4.8	-
Nose (km)	30.4 ± 15.3	31.5 ± 14.9	20.6 ± 6.7	27.0 ± 7.7	19.3 ± 3.7	18.7 ± 6.2	19.3 ± 3.5
Nose Rainy	33.4 ± 29.7	30.1 ± 29.5	17.2 ± 4.5	29.2 ± 12.0	17.2 ± 1.2	18.4 ± 9.0	19.3 ± 3.5
Nose Dry	29.4 ± 12.0	31.9 ± 11.1	24.6 ± 6.9	25.5 ± 2.9	20.5 ± 4.3	18.9 ± 5.0	-
Core (km)	15.5 ± 5.3	16.3 ± 6.4	11.7 ± 5.1	13.8 ± 2.2	9.4 ± 4.0	7.9 ± 5.6	9.4 ± 1.6
Core Rainy	16.2 ± 13.3	12.7 ± 14.9	8.9 ± 3.5	11.8 ± 1.5	6.9 ± 0.9	6.9 ± 8.2	9.4 ± 1.6
Core Dry	15.3 ± 2.2	17.5 ± 2.6	15.1 ± 4.8	15.3 ± 1.2	10.9 ± 4.5	8.5 ± 4.2	-

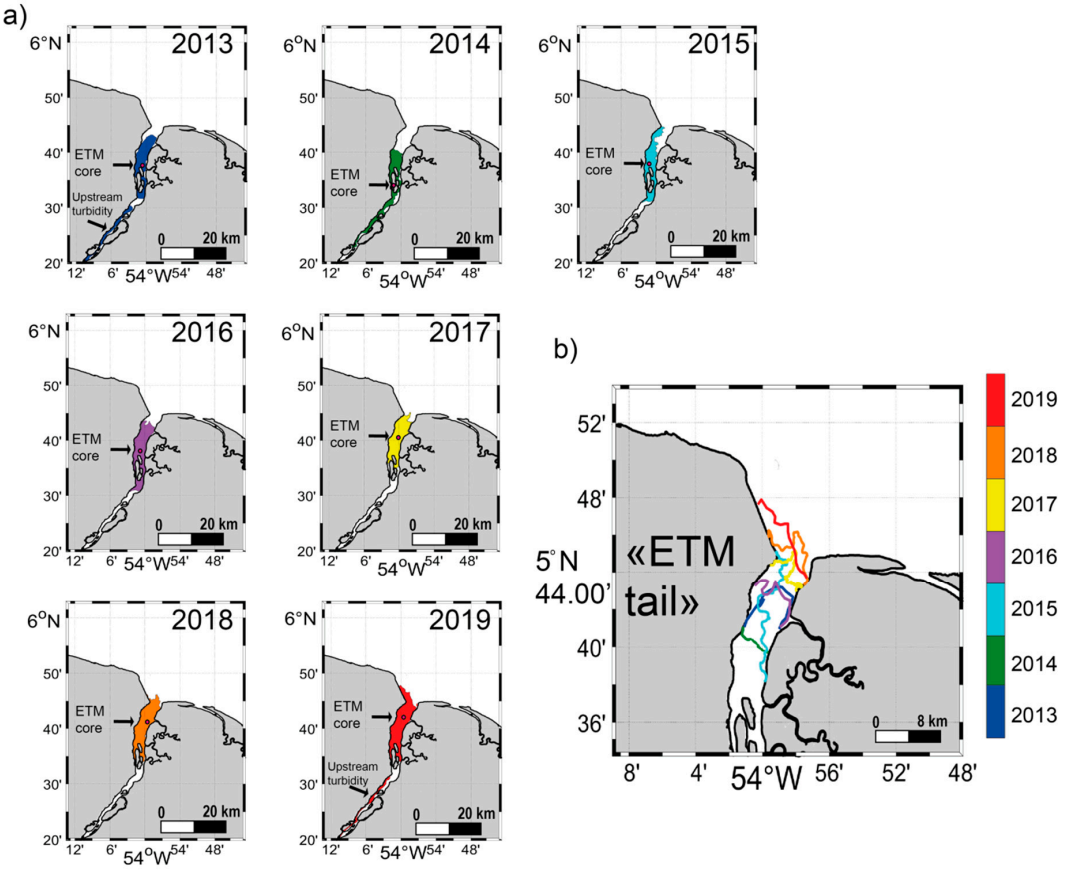

Figure 3. Spatiotemporal distribution of the ETM from 2013 to 2019 (**a**) Demarcation of the ETM "tail"estimated following criteria explained in Section 2.2.4. (**b**) The ETM location is representative of the average situation for each year, which was estimated using the number of scenes presented for each year in Table 1. The pink dot represents the core of the ETM.

The results for each of the years are depicted in Figure 3 and Table 2. The area of the ETM (Table 2) shows an increase in 2018 and 2019, with values of 69.4 ± 19.9 and 76.6 ± 28.7 km^2, respectively. The ETM "tail" was found near the coast (KP 0) in the last three years of the study (2017–2019) (Figure 3a,b and Table 3). The shift of the averaged ETM "tail" towards the mouth of the estuary for those years coincides with the increase in ETM extension for the years 2018 and 2019. The ETM "nose" (Figure 3a and Table 3) also experienced a migration of 9.6 km after 2014. However, none of the forcing agents (Figure 2) has experienced a shift in tendency since 2017 (the year with the longest rainy season), a fact that could have explained a high resuspension of SPM.

Even though significant wave heights show a decreasing trend until the year 2018 (Figure 2e), the location of the ETM does not seem to be affected by the high wave heights between 2013 and 2015. However, the important offshore wave height decrease experienced between 2015 and 2016 could explain the absence of the ETM at the west bank of the Maroni estuary for 2016 (between KP 0 and KP4.6) contrary to 2015 and 2017 (Figure 3a-2016), which show shallow bathymetry values (Figure 1c). Gratiot et al. [27] established a clear link between increases and decreases in wave heights and SPM. The direct exposure of the west bank to the prevailing waves from east to northeast could explain significant mud resuspension and alongshore mobilization, and hence the absence of an ETM. In 2014, the ETM showed a length of 40.9 km (from the "tail" to the "nose"), the longest in the course of the study period. This length could be related to the low discharge values in 2014. Low discharge is known to induce landward shifts of the ETM [52].

For the years 2019 and 2013, another area of maximum turbidity, quite distinct from the classical ETM, is observed upstream (Figure 3a-Upstream turbidity). The presence of an upstream turbidity area

in the Maroni River could be related to fluvial sediment influx as it occurs in the rainy season when runoff values are high [44]. It should be noted, however, that the presence of this river turbidity zone for 2019 goes with the availability of only rainy season scenes for this year (Table 1). Therefore, the situation in 2019 is representative only of that year's rainy season. Following the spatial patterns found for the rainy and the dry season (Table 3), we could expect that the ETM during the dry season of 2019 will undergo a landward "tail" and "nose" shift. Conversely to that situation, the available scenes for 2013 correspond to both seasons (Table 1), with a better representation of the dry season for that year. Despite that, a river turbidity zone is still observed upstream (Figure 3a, 2013: Upstream turbidity). This same situation is, as already mentioned, also observed in 2014, when the ETM was present all along the west bank of the river (Figure 3a, 2014), between 7.4 ± 6.1 and 31.5 ± 14.9 km upstream of KP 0 (Table 3). SPM values inside the ETM during 2014 are lower than during 2013 (not shown) and more heterogeneous, and this could be related to the lower 2014 river discharge values compared to those of 2013 (Figure 2b). Even though the dry and the rainy season are better represented by the years 2013 and 2019, respectively, these spatial patterns, depicted in Figure 3, allow us to evaluate the evolution of the location of the ETM over a period of six years, which corresponds to about 20% of the time necessary for a mud bank to go past a given location [53]. In this case, the years 2013–2019 are within the range of the first years of encroachment of the mud bank.

During both the rainy and the dry seasons, the averaged extension and location of the ETM show similar values (Tables 2 and 3). However, although the extension and ETM "tail" and "nose" are similar, the ETM core migrated landward from the rainy to the dry season (with the exception of the year 2013) (Table 3). Sottolichio et al. [15] showed that the salt intrusion during the rainy season could go up to ~5 km upstream from the mouth of the Maroni in the rainy season and ~12 km during the dry season, these values being similar to those identified by Jouanneau and Pujos [33] (~5 and ~11 km, respectively) over three decades ago. Even though these are rough estimates, the variation of the salt intrusion between both seasons could explain the landward migration of the core of the ETM.

3.2. Tidal Influence

Averaged SPM-normalized values were estimated to evaluate the tidal influence on the ETM's spatial location. This influence is analyzed in Figure 4 for both seasons.

During neap tides, the ETM is located between KP 6.2 and KP 27.2 (Figure 4a,b), and increasing SPM-normalized concentrations from ~0.62 ± 0.31 to 0.93 ± 0.76 are observed from the upstream part of the ETM to its downstream part. The core location of the ETM during the dry season is 14.8 ± 2.6 km compared to the mean location of 14.1 ± 6.4 km in the rainy season, thus highlighting a more stable ETM core position during the dry season (Figure 4a,b). High SPM-normalized concentrations are observed all along the ETM during the rainy season, with average values of ~0.76 ± 0.39. A river turbidity maximum is observed during this season at the west bank of the river 29.5 km from KP 0 (Figure 4b). High SPM concentrations are found in this river turbidity maximum, with averaged SPM-normalized values of 0.87 ± 0.62 (Figure 4b).

During spring tides, the ETM is located between KP 0 and KP 25.3 (Figure 4c,d), and it is longer than during neap conditions (Figure 4a,b). The dry season is characterized by an ETM with a core position of 10.2 ± 5.8 km, whereas the rainy season shows a position of 9.9 ± 6.9 km. SPM-normalized concentrations exhibit a longitudinal variation, with an increase from the west in the downstream area (~0.76 ± 0.49) (between KP0 and KP10) to the east in the area surrounding the downstream islands (~0.81 ± 0.52) (islands between the KP 1 0 and KP20) (Figure 4c). High SPM-normalized concentrations are found in the coastal area of the estuary and outside the ETM, with mean values of ~0.43 ± 0.26 (Figure 4c). The ETM during the rainy season has a length of 22.3 km, and up to 3.1 km of the ETM length is located in the coastal area of the estuary (after KP 0) (Figure 4d). Averaged SPM-normalized concentrations are uniform at both banks of the estuary, with a mean value of 0.72 ± 0.21, whereas averaged SPM at the coastal area of the estuary and seaward of the ETM (after KP 0) shows a value of ~0.47 ± 0.27 (Figure 4d).

Tidal currents seem to play a major role in the spatial variability of the ETM during both seasons. However, river discharge seems to modify the ETM "nose" and "tail" positions, which, for both neap and spring tides, are downstream for high river discharge conditions. These results are consistent with those obtained by Sottolichio et al. [15], who showed that SPM concentrations were influenced more by tidal currents during the dry season, whereas they were influenced more by river discharge during the rainy season.

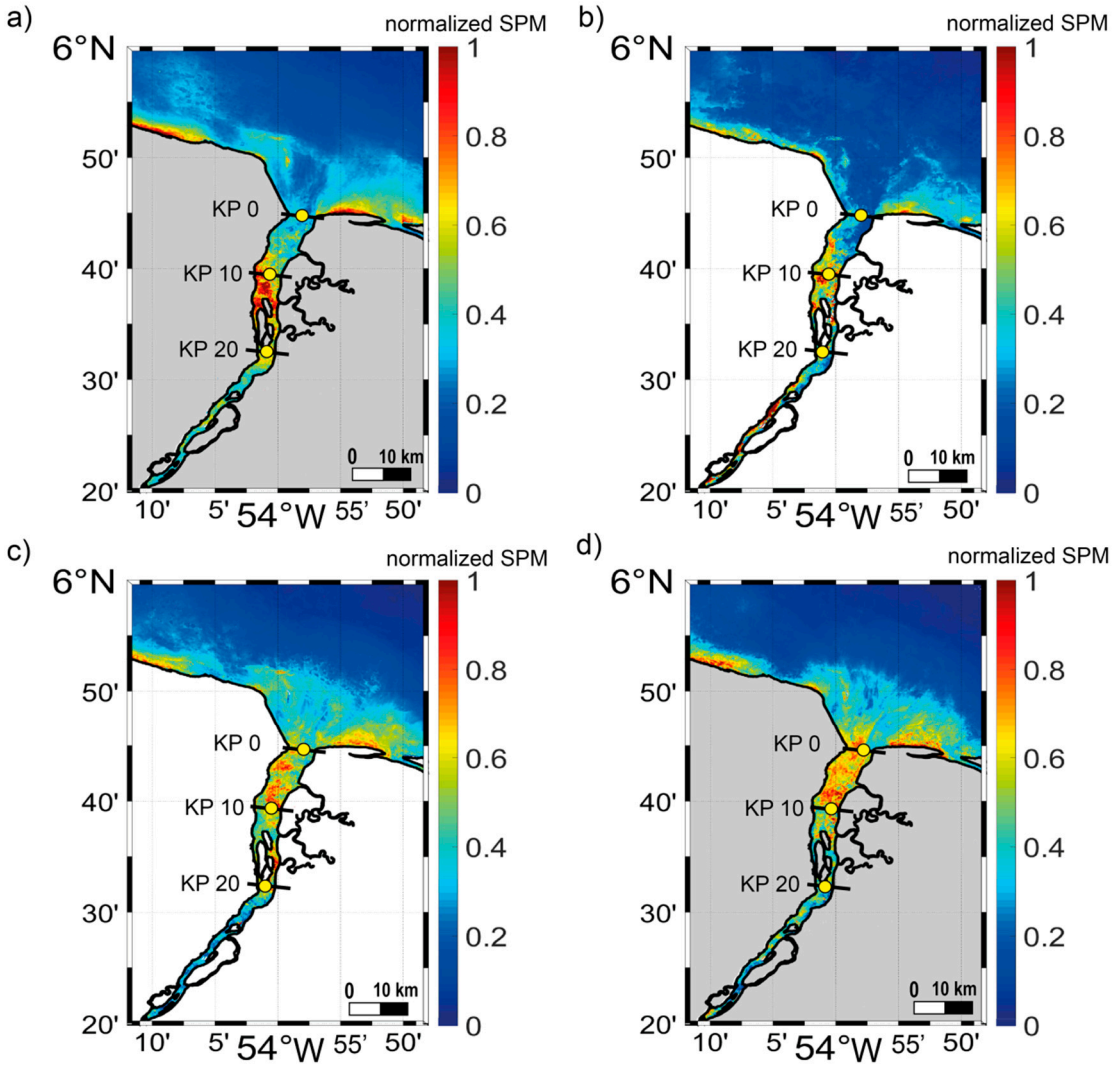

Figure 4. Averaged normalized SPM for neap tides during (**a**) the dry (a total of 20 scenes) and (**b**) the rainy season (a total of 11 scenes) and spring tides during (**c**) the dry (a total of 12 scenes) and (**d**) the rainy season (a total of 18 scenes) for the period between 2013 and 2019. SPM values are normalized following the criteria presented in Section 2.2.4 and are representative of the average SPM conditions for the images with different tidal conditions.

During neap tides, SPM values inside the ETM zone are higher for the rainy season, 170.9 mg/L, than for the dry season, 113.76 mg/L. This difference could be explained by the inter-annual variation of river discharge, as during the dry season the decrease in discharge would allow the development of a well stratified water column that can impede resuspension [54].

3.3. River Discharge

As the mixing zone normally occurs near the limit of the salt intrusion [55,56] and the salt intrusion depends on the magnitude of river discharge and tidal range [57], the influence of river discharge on the ETM's spatial location is presented in Figure 5.

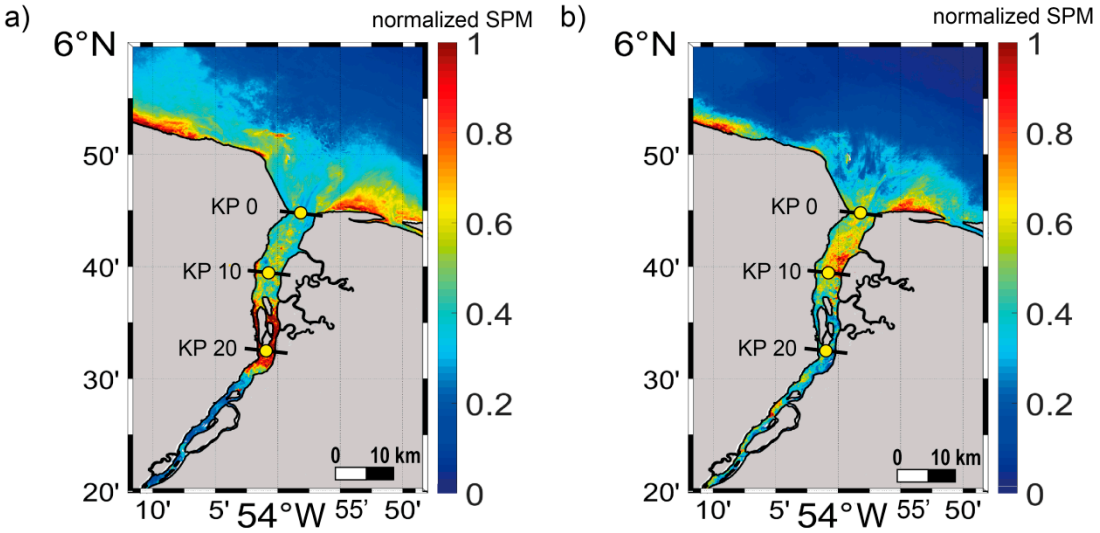

Figure 5. Averaged normalized SPM for (**a**) low and (**b**) high discharges calculated for the scenes when river discharge is below 500 m^3/s (14 images) and above 2000 m^3/s (13 images), respectively. SPM values are normalized following the criteria presented in Section 2.2.4 and are representative of the average SPM conditions for images with different river discharge conditions.

For the scenes characterized by a river discharge lower than 500 m^3/s (corresponding to the 15th percentile of the river discharge values for the period 2013 to 2019), this location is situated in the area of the downstream vegetated islands (between KP 15.2 and KP 26.5). Near the mouth of the estuary, averaged SPM-normalized values are high at the west bank (Figure 5a), where the bathymetry is relatively shallow (Figure 1c). Averaged SPM-normalized values inside the ETM are very homogeneous, with a mean of ~0.92 ± 0.47, which corresponds to a mean value of 146.4 mg/L (estimated as the mean value of the pixels inside the ETM zone using the corresponding non- normalized SPM maps, see Section 2.2.5). In the coastal area, the influence of the channel is detected, manifested by low values of averaged normalized SPM where the bathymetry is deep [36], whereas values of ~0.52 ± 0.22 are present at the shallower east and west sides of the channel.

During high flow conditions (exceeding 2000 m^3/s, as in the case of the study of Berthois and Hoorelbeck [58]), the ETM is located between the mouth of the estuary (KP 0) and the downstream zone of the islands (KP 15.4) (Figure 5b). Averaged SPM values exhibit a heterogeneous distribution (Figure 5b) as maximum values are observed at the east bank of the river (between KP 7.5 and KP 10), over an area with shallow bathymetry (Figure 1c). The rest of the ETM exhibits an almost constant SPM-averaged value (~0.67 ± 0.35). During high river discharge conditions, both the coastal and the upstream areas of the estuary (outside the ETM) exhibit high normalized SPM, with averages of 0.36 ± 0.31 and 0.55 ± 0.27, respectively. In the coastal area, high SPM values are observed in the area with the deepest bathymetry as reported by Jolivet et al. [36].

The annual variation of river discharge, which reached a minimum of 146 m^3/s and a maximum of 6670 m^3/s for the period of study (Figure 2b), is consistent with the seasonal variation in the location of the ETM. Under high river discharge, relatively high SPM values are observed at the upstream part of the estuary, especially at the west bank (Figure 5b). Even though the suspended sediment supply of French Guiana rivers [42], and the Maroni River in particular, is low, the sharp increase in anthropogenic activities over the last decade, notably gold mining in this river's catchment, especially

along the border with Suriname [44], could explain the relatively high values along the west bank of the river during these high river flow conditions.

3.4. SPM and Variability of ETM Extension Due to External Conditions

SPM values inside the estuary are the result of the combination of different sources of dynamic forcing; nevertheless, the previous results correspond to a synthesis for different dynamic conditions. To better analyze these differences and the influence of these dynamic conditions, SPM values under different tidal, river discharge, wind and wave conditions are presented in Figure 6. Contrasting dynamics are observed for neap tides during ebb and flood (Figure 6b,c,f). During ebb tides, the ETM is well developed (Figure 6b,f) and is located in the area between the downstream islands (KP 20and KP 0). High values of SPM are observed at the west bank of the estuary, which has been identified as the ebb channel [16], especially for 2018, when the length of the ETM was considerably longer than that of 2014 (Figure 6b,f). This is consistent with the results of Jolivet et al. [36]: the dominant direction of transport of sediments from this river is westwards along the Suriname coast. During flood, a clear ETM at the surface of the water column is absent in the estuary (Figure 6c). This would suggest a stratification of the water column for this scene of the dry season. As a consequence of this stratification, high resuspension of SPM is impeded [54] and low SPM values are observed at the surface of the water column (Figure 6c). Therefore, flood tides are characterized by low SPM values in comparison to ebb tides, as observed by Asp et al. [59] in a river on the coast of Para State in North Brazil, also under the influence of the Amazon. No clear influence of wind velocity values is detected when the different scenes are compared (Figure 6).

During spring tides, SPM-averaged values inside the ETM are higher than during neap tides (Figures 4 and 6) for both seasons. During the dry season, these values reach 160.6 mg/L, whereas they attain 195.6 mg/L during the rainy season. Likewise, at neap tides, ebb tides present a clearly delineated ETM located at the mouth of the estuary (Figure 6e). Even though the river discharge is 3.7 times lower in Figure 6a than in Figure 6e (545 and 2030 m^3/s, respectively), and both scenes correspond to ebb tides, SPM values exhibit a slight longitudinal variation and are high (~210 mg/L) (Figure 6a). This could be related to the river discharge, as even though the daily value for that date is relatively low (545 m^3/s), an increase in discharge is observed in the days prior to 24 December 2014 (Figure 2a). The increase in river flow could have enhanced suspended sediment remobilization after a period of low river discharge, thus leading to the high SPM along the river and estuary when compared to the other ebb scene (Figure 6e). SPM at the coastal area in front of the estuary is also characterized by high values (averaged SPM of 96.9 mg/L) when compared to neap tide values (averaged SPM of 44.8 mg/L) (Figure 6). During these tidal conditions, high resuspension characterizes the sand-filled estuary mouth with its various shoals and banks (Figure 6a,e). The area surrounding the vegetated islands (Figure 1c) exhibits relatively high flood-tide SPM values (~110 mg/L) and the flood channel is clearly identified at the mouth of the estuary (Figure 6d). In the coastal area of the estuary, high resuspension prevails, especially at the shallow west side of the flood channel [36].

The impact of the river on the mud bank is also illustrated in Figure 6. River discharge impacts the subtidal resuspension of muddy deposits at the east bank in the coastal area of the estuary (Figure 6b,c,f). This confirms the influence of large rivers such as the Maroni on mud banks, as the river discharge, even in low-flow conditions (Figure 6c,d,f), seems to generate a hydraulic-groyne effect that slows down mud-bank migration through mud fluidization [31], inducing muddy accretion on the updrift sector of the estuary mouth [36]. However, such impedance of mud-bank migration across the Maroni estuary mouth would not only impact migration rates, but could also lead to some mud being displaced up the estuary [14].

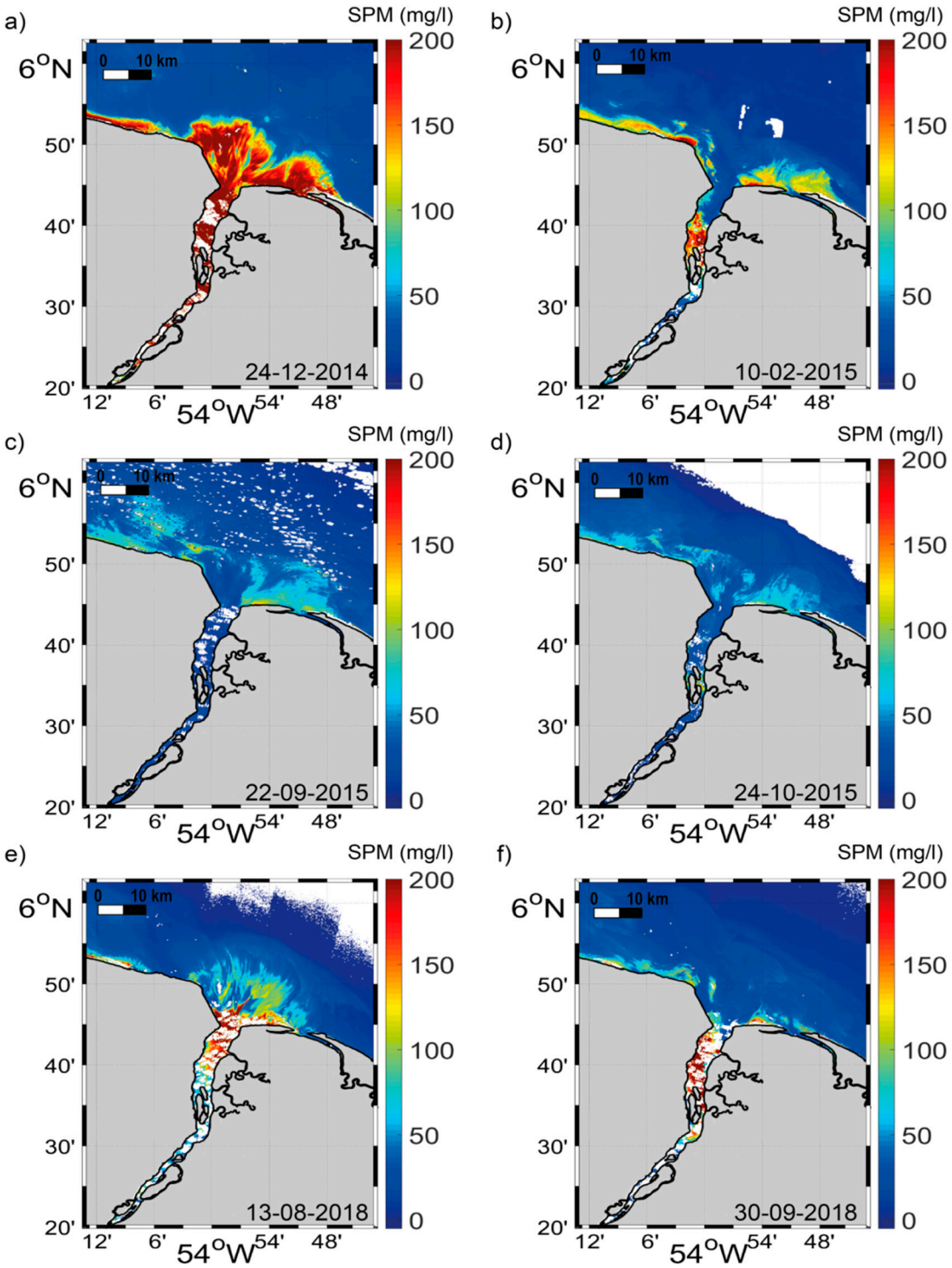

Figure 6. SPM values (mg/L) for available images confronted with values for different tidal, river discharge and wind conditions. (**a**) Image corresponding to spring ebb tide, with a river discharge of 545 m^3/s, a wind speed of 6.72 m/s and a wave height of 1.56 m. (**b**) Image corresponding to neap ebb tide, with a discharge rate of 1040 m^3/s, a wind speed of 3.83 m/s and a wave height of 1.77 m. (**c**) Image corresponding to neap flood tide, with a discharge rate of 486 m^3/s, a wind speed of 7.48 m/s and a wave height of 1.16 m. (**d**) Image corresponding to spring flood tide, with a discharge rate of 211 m^3/s, a wind speed of 8.4 m/s and a wave height of 1.08 m. (**e**) Image corresponding to spring ebb tide, with a discharge rate of 2030 m^3/s, a wind speed of 6.35 m/s and a wave height of 0.93 m. (**f**) Image corresponding to neap ebb tide, with a discharge rate of 778 m^3/s, a wind speed of 6.97 m/s and a wave height of 1.50 m.

SPM dynamics in the estuary have been observed (Figure 6) to be largely variable, with an ETM that is not always well developed (Figure 6a,c). As shown in Tables 2 and 3, the ETM extension and the locations of its "tail", "nose" and "core" exhibit relatively high standard deviations relative to their averaged values for some of the years and seasons. To enhance our analysis of the variation of the ETM extension in response to the different dynamic forcings, we confronted these averaged values to values of river water discharge, tide, wave height and wind corresponding to each image. Figure 7 depicts relationships covering a number of situations.

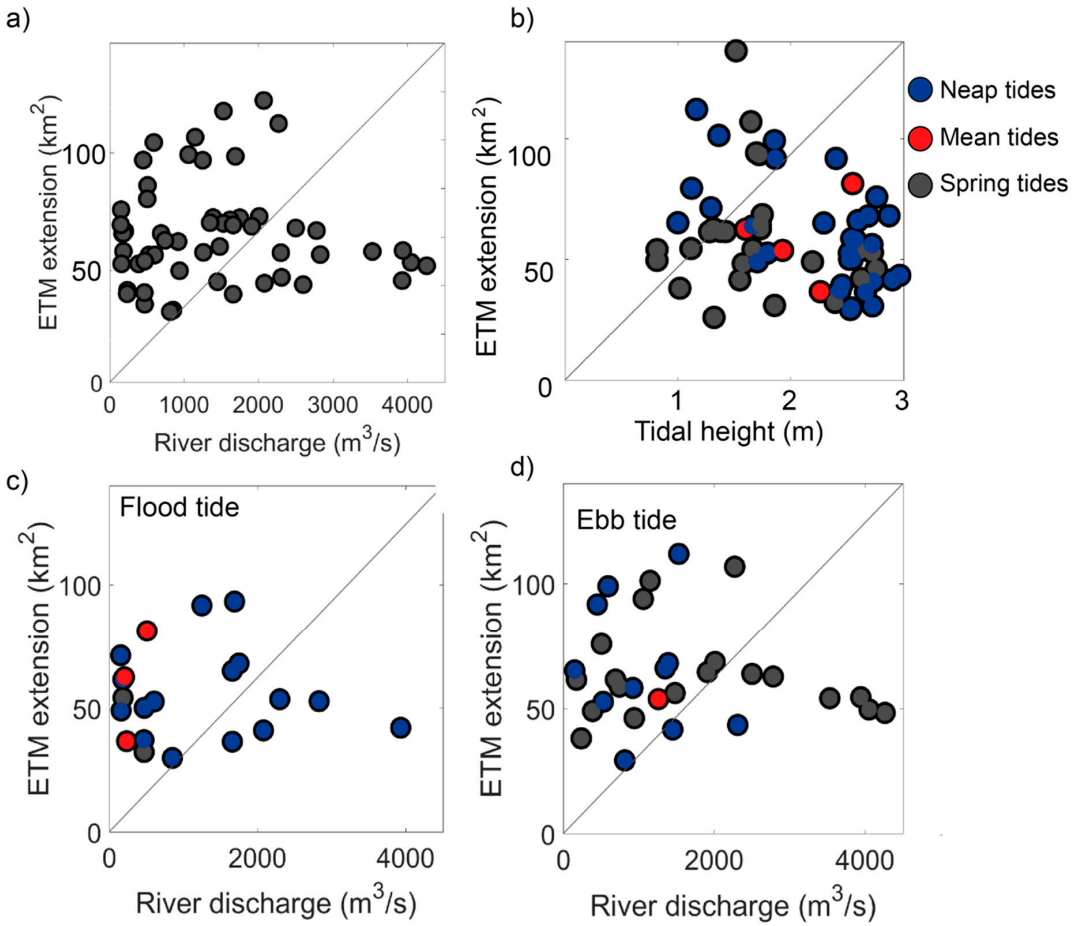

Figure 7. Comparison of the ETM extension (in km^2) with two dynamic drivers, river discharge and tides. (**a**) ETM extension and river discharge. (**b**) ETM extension and tidal height values for all tides. Blue dots correspond to images characterized by neap tides, red dots by mean tides and grey dots by spring tides as explained in Section 2.2.5. (**c**) ETM extension compared to flow rate values for those images presenting flood tide and (**d**) compared to those images presenting ebb tide.

River discharge (Figure 7a) displays a better correlation (R = 0.41, p = 0.12) than wind velocity or wave height (R = −0.35, p = 0.38; R = 0.05, p = 0.66, respectively) (not shown in the figure), neither of which seems to be effective in determining ETM extensions. However, given the moderate relationship between river discharge and ETM, it is clear that this dynamic agent is not the sole driver of ETM extension. For those images corresponding to a discharge of < 500 m^3/s, the ETM extension ranges from 32.2 to 91.7 km^2 (Figure 7a). The same is observed when images with a discharge > 2000 m^3/s are considered; the range variability of ETM extension goes from 40.3 to 63.7 km^2 (Figure 7a). In the case of the tide, a clearer tendency emerges (R = −0.31 and p = 0.015), especially when the tidal range is < 2 m (Figure 7b). As the previous section shows that both tide and flow rate highly modulate the variations and location of the ETM, its extension is compared to the flow rate for those images presenting flood and ebb conditions (Figure 7c,d). ETM extension for both tidal situations varies with the flow rate,

increasing when this value does (Figure 7c,d). However, this tendency is not that clear when discharge values are higher than 2500 m^3/s for both tidal conditions, and lower than 500 m^3/s, especially for flood conditions (Figure 7c,d).

In the case of the images associated with ebb conditions and high river discharge, the almost constant value of ~50 km^2 for the extension of the ETM could be related to both high discharge and ebb tide currents pushing the ETM seaward, inducing a limitation of its development to the mouth of the estuary. For flood conditions and low discharge, it seems that images capturing the early hours of the ebb tide depict a larger extension that those closer to low tide (figure not shown). However, it is observed that the dynamics affecting the ETM extension are really complex, as no clear relationship among them comes out, even when they are combined. This could be related to the stratification of the water column and how it affects what can be detected from the water surface.

3.5. Medium-Term (2013–2019) Variation: The Influence of Periodic Amazon-Derived Mud Banks

Although an overall increase in SPM values in the Maroni River has been observed since 2009 [44], the SPM increase in the upstream area seems too small to justify the increase in ETM extension between 2013 and 2019 (Table 2). Moreover, river discharge seasonality alone cannot explain this extension, as mean SPM values for 2016, for example, were ~30 mg/L for all upstream Maroni stations [44]. Therefore, the sediment source is likely to be related to the mud bank present in the study area since 2011, reflecting a situation similar to that reported by Orseau et al. [14] for the smaller Mahury estuary in eastern French Guiana. This influence is observed in the increasingly more seaward position of the ETM "tail" (Figure 3b and Table 3). This seaward position could be related to the mud-bank migration process. The back (trailing edge) of the bank is composed of semi-consolidated mud that is eroded and fluidized by waves, tidal currents and wind-induced geostrophic currents [60,61]. Tidal current speeds at the east bank of the Maroni estuary mouth exceed 0.75 m/s during ebb and 1 m/s during flood [36], which correspond to velocities that can initiate erosion [62,63], in addition to wave attack [27]. The erosion of the back of the bank could provide the extra amount of mud for injection into the Maroni's ETM, as also suggested by Jolivet et al. [36].

In support of the fore-going observations on the location and extension of the ETM (Tables 2 and 3), SPM values have increased downstream since 2013 (Figure 8). At station S1, located at the mouth of the estuary (Figure 1b), mean SPM values have undergone an increase of ~128 mg/L since 2013 (Figure 8a), and of ~ 259 mg/L at station S2 (Figure 8b). Considering the mud-bank front (leading edge) position for year 2017 [36] and a migration speed of about 2.3 km/year [29], the subtidal part of the mud bank (which forms the bulk of a mud bank [14,38]) has been crossing the estuary mouth since 2017. Different features, such as the increase in SPM, extension of the ETM, and the clear seaward evolution of the ETM "tail" since 2017 (Table 3), could then be explained by the migration of the mud bank across the estuary mouth. As the evolution and spatial patterns of the ETM are mainly modified by river discharge and by tide-induced transport, these would be the principal drivers of mud intrusion into the estuary, as also suggested by Orseau et al. [14]. Landward mud ingression has also been identified as the main source of sediments in other estuaries under the influence of the Amazon River plume [59], confirming the influence of muddy deposits from the Amazon in the sediment dynamics and potential long-term infill of estuaries in northern South America. It may be expected that, during inter-bank phases separating mud-bank phases, these Amazon-influenced estuaries would have a functional regime similar to that of other tropical estuaries elsewhere, with minimal influence of outside mud-sourcing.

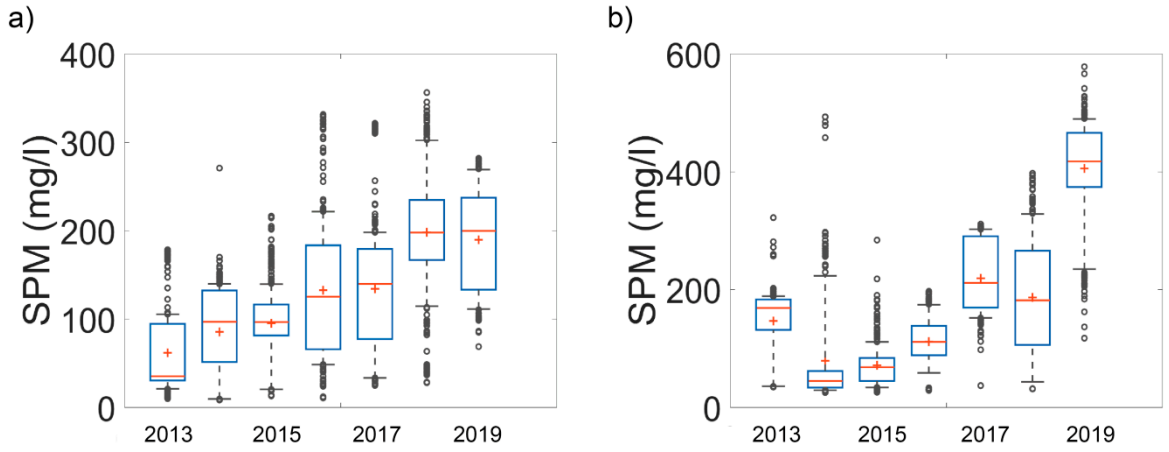

Figure 8. Evolution of SPM values at two different downstream estuarine stations: (**a**) S1; and (**b**) S2 (Figure 1b). Median (red line), mean (red cross), 25th and 75th percentile (blue bars) values and 9th and 91st percentile values (horizontal black lines) of SPM for the period of study between 2013 and 2019.

3.6. Capacity of Satellite Images in Contributing to Analysis of Estuarine Dynamics

The spatial resolution of data from the new generation of satellite images for ocean color, such as Landsat 8 (30–15 m; used in this study), has enabled us to attempt to characterize the spatial evolution of the ETM, using for the first time six-year time series data in a tropical estuary. Although the methods used in the present study have enabled an exploratory characterization of the seasonality of the ETM and the influence of tidal currents and of an external source of mud, namely, an Amazon-derived mud bank, the temporal resolution of Landsat 8 satellite images (16 days) is a limiting factor in gaining insight into small temporal-scale processes. The number of available images (Table 1) is restricted due to the high cloud cover in this equatorial area. This limited temporal coverage could affect our comprehension of the seasonal differences in the study area, as only a small number of rainy season images can be exploited (Table 1), a period when high river discharge considerably impacts ETM dynamics. The inter-annual variation of the ETM is, thus, highly hinged on the available scenes, the dry season being much better represented than the rainy season (Table 1). This, therefore, constitutes a limitation in the analysis. For 2019, only rainy season scenes were selected. An upstream river turbidity maximum was detected that year. This maximum appears also in 2013 and 2014, indicating that river influence becomes appreciable only under certain dynamic conditions (Figures 3a and 7).

The recently-launched Sentinel 2 missions, with a spatial resolution of 10 m and a time resolution of five days, will allow for greater insight into the ETM, as the combination of data from this satellite and from Landsat 8 will generate a much higher temporal resolution. This higher resolution should allow for a better characterization of occasional (or semi-permanent) features such as the river turbidity maximum observed upstream in the Maroni. It should also enable us to identify the influence of different drivers of mud-bank migration and sediment resuspension, such as oceanic currents and trade-wind waves [27,28,64], as well as better characterization of resuspension processes at the sand-filled estuary mouth of the Maroni and at the back of the mud bank. These processes cannot presently be explained using the Landsat 8 series only. One current limitation of reliance on satellite data is that only surface SPM patterns are apprehended. It would, thus, also be necessary to compare these surface results with in-situ values of SPM in the water column. This comparison should enable a better explanation of the dynamics of the ETM, comparing them also to the tidal excursion between neap and spring tides and the influence of the limit of salt intrusion related to the stratification of the water column in tropical estuaries under the influence of the Amazon. It would also be necessary to compare these results with those derived from hydro-sedimentary models that provide a better description of mixing processes for different dynamic forcing conditions.

4. Conclusions

Understanding the spatial and temporal variability of the ETM is of primary importance in tropical estuaries where studies focusing on the sediment dynamics are rare, whereas development needs, including estuarine navigation, port development and monitoring of river-to-coast pollution, are rising with population increase. The dynamics of the Maroni estuary are representative of that of tropical-equatorial estuaries subject to strongly seasonal discharge, but this study also illustrated the idiosyncratic character of Guiana Shield estuaries, generally poor in intrinsic mud supply from their crystalline catchments, but periodically subject to extraneous mud under the influence of the Amazon River and its massive muddy discharge into the coastal ocean of northern South America. Many of these Guiana estuaries are also undergoing changes in sedimentation patterns caused by human activities and deforestation upstream, while port facilities are being actively developed. Our study illustrated the potential of time series obtained using high-resolution sensors, such as Landsat 8-OLI, for characterizing the ETM of a tropical estuary and the periodic influence of Amazon mud banks on this feature, notwithstanding the complexity of ETM detection using surface SPM values without a consideration of depth concentration gradients. Satellite data are, indeed, proving to be an effective tool for monitoring coastal areas with very turbid waters, such as the Guianas coast [27,29,38,65,66] where field monitoring is a challenging task.

SPM values were obtained using a general algorithm that allows the estimation of four ranges of SPM magnitude. The estimates were normalized and image pixels that presented a value >0.6 were retained to yield an envelope of values that was used to identify the ETM zone. This methodology allowed for the definition of the ETM under different dynamic conditions and the characterization of tropical seasonality, inter-annual variations and the influence of tides and river discharge on the ETM. This study evidenced an ETM variation influenced by the well-marked seasonal river discharge and the neap–spring tidal cycle, especially during the dry season, as observed in Sottolichio et al. [15]. As a result, the ETM is located in the estuary mouth during high river discharge conditions and it shifts inwards towards the middle estuary during low flow conditions. Neap–spring tidal range variations result in a push of the ETM closer to the mouth of the estuary under spring-tide conditions or even outside the mouth during spring tides in the rainy season.

The influence of the migration of a mud bank present at the mouth of the Maroni since 2011 was also observed. The ETM is pushed towards the coastal area of the estuary as the mud bank migrates across its mouth. An increase in SPM values is also observed within the ETM zone, as well as an increase in ETM extension. This study confirms observations made in a previous study in the area that highlighted the role of alongshore migrating Amazon-derived mud banks as purveyors of sediments that intrude into the estuaries of the Guianas [14]. Thus, an important source of mud for the Maroni estuary, a river with a catchment considered as a rather poor purveyor of mud, is likely to be offshore and related to the periodic passage of mud banks “en route” from the Amazon to the Orinoco. To determine to which extent Amazon mud scales relative to the intrinsic mud derived from the Maroni catchment in the constitution of the estuary’s ETM would require a set of observations and analyses conducted during an inter-bank period, when coastal waters under the influence of the Amazon are characterized by relatively low turbidity in the vicinity of the Maroni.

The results obtained provide new perspectives for the analysis of tropical estuaries through satellite data and estimates derived thereof, such as SPM, and for the identification of the spatial and temporal evolution of the ETM in relation to tidal, seasonal and inter-annual regimes. Even though Landsat-8 presents a low revisit frequency, the methodology used and the results obtained are very promising for studying coastal and estuarine areas. The combination of data from this satellite with data from the Sentinel-2A and -2B satellites recently launched by the European Space Agency will make for considerable enhancement of knowledge on the inter-annual and seasonal variability of ETM zones. The application of this analysis to Sentinel 2 data will enable better characterization of the ETM during the rainy season and provide significant advantages in the observation of short timescale processes. Moreover, augmentation of the quantity of data would enable a determination

of the influence of wind-induced waves and currents on SPM values and ETM evolution, the main drivers of coastal suspended sediment dynamics on the Guianas coast [27,64]. Better knowledge of the short-term processes could benefit from integration with in-situ measurements and hydro-sedimentary models, providing a more thorough description of mixing processes for different dynamic forcing conditions, and a valuable aid to estuarine management scenarios under increasing human pressures and climate change.

Author Contributions: Conceptualization, N.A.-Z., V.V., N.H., E.J.A. and A.G.; Methodology, N.A.-Z. and V.V.; Software, N.A.-Z., V.V. and D.D.N.; Validation, N.A.-Z. and V.V.; Investigation, N.A.-Z., V.V., N.H., E.J.A. and A.G.; Writing—original draft preparation, N.A.-Z.; Writing—Review and editing, E.J.A., N.H., V.V. and A.G.; Supervision, E.J.A., V.V., N.H. and A.G.; Project administration, V.V., N.H. and A.G.; and Funding acquisition, V.V., N.H. and A.G. All authors have read and agreed to the published version of the manuscript.

Funding: This research was funded by the co-funding of N. AbascalZorrilla's PhD thesis by the CNES, under the HARDECOT TOSCA project, DEAL Guyane and Grand Port Maritime de Guyane. Funding was also provided by the European Fund for Regional Development (ERDF) program OYAMAR and by the French Guiana Office of Water under the EFHEMAR project. The APC was funded by CNRS.

Conflicts of Interest: The authors declare no conflict of interest.

References

1. Dyer, K.R. Fine Sediment Particle Transport in Estuaries. In *Physical Processes in Estuaries*; Dronkers, J., Van Leussen, W., Eds.; Springer: Berlin/Heidelberg, Germany, 1988; pp. 295–310. [CrossRef]
2. Ganju, N.K.; Schoellhamer, D.H.; Warner, J.C.; Barad, M.F.; Schladow, S.G. Tidal oscillation of sediment between a river and a bay: A conceptual model. *Estuar. Coast. Shelf Sci.* **2004**, *60*, 81–90. [CrossRef]
3. Islam, M.S.; Ueda, H.; Tanaka, M. Spatial distribution and trophic ecology of dominant copepods associated with turbidity maximum along the salinity gradient in a highly embayed estuarine system in Ariake Sea, Japan. *J. Exp. Mar. Bio. Ecol.* **2005**, *316*, 101–115. [CrossRef]
4. Woodruff, J.D.; Geyer, W.R.; Sommerfield, C.K.; Driscoll, N.W. Seasonal variation of sediment deposition in the Hudson River estuary. *Mar. Geol.* **2001**, *179*, 105–119. [CrossRef]
5. Milliman, J.D.; Syvitski, J.P.M. Geomorphic/tectonic control of sediment discharge to the ocean: The importance of small mountainous rivers. *J. Geol.* **1992**, *100*, 525–544. [CrossRef]
6. Victor, S.; Golbuu, Y.; Wolanski, E.; Richmond, R.H. Fine sediment trapping in two mangrove-fringed estuaries exposed to contrasting land-use intensity, Palau, Micronesia. *Wetl. Ecol. Manag.* **2004**, *12*, 277–283. [CrossRef]
7. Van Santen, P.; Augustinus, P.G.E.F.; Janssen-Stelder, B.M.; Quartel, S.; Tri, N.H. Sedimentation in an estuarine mangrove system. *J. Asian Earth Sci.* **2007**, *29*, 566–575. [CrossRef]
8. Willemsen, P.W.J.M.; Horstman, E.M.; Borsje, B.W.; Friess, D.A.; Dohmen-Janssen, C.M. Sensitivity of the sediment trapping capacity of an estuarine mangrove forest. *Geomorphology* **2016**, *273*, 189–201. [CrossRef]
9. Anthony, E.J. Sediment dynamics and morphological stability of estuarine mangrove swamps in Sherbro Bay, West Africa. *Mar. Geol.* **2004**, *208*, 207–224. [CrossRef]
10. Wolanski, E. Hydrodynamics of mangrove swamps and their coastal waters. *Hydrobiologia* **1992**, *247*, 141–161. [CrossRef]
11. Simpson, J.H.; Gong, W.K.; Ong, J.E. The determination of the net fluxes from a mangrove estuary system. *Estuaries* **1997**, *20*, 103–109. [CrossRef]
12. Kitheka, J.U. Coastal tidally-driven circulation and the role of water exchange in the linkage between tropical coastal ecosystems. *Estuar. Coast. Shelf Sci.* **1997**, *45*, 177–187. [CrossRef]
13. Capo, S.; Sottolichio, A.; Brenon, I.; Castaing, P.; Ferry, L. Morphology, hydrography and sediment dynamics in a mangrove estuary: The Konkoure Estuary, Guinea. *Mar. Geol.* **2006**, *230*, 199–215. [CrossRef]
14. Orseau, S.; Lesourd, S.; Huybrechts, N.; Gardel, A. Hydro-sedimentary processes of a shallow tropical estuary under Amazon influence. The Mahury Estuary, French Guiana. *Estuar. Coast. Shelf Sci.* **2017**, *189*, 252–266. [CrossRef]
15. Sottolichio, A.; Gardel, A.; Huybrechts, N.; Maury, T.; Morvan, S.; Lesourd, S. Premières Observations De La Dynamique Hydro-Sédimentaire De L'Estuaire Du Maroni (Guyane). In Proceedings of the XV National

Conference on Coastal and Civil Engineering (GCGC), La Rochelle, France, 28–31 May 2018; pp. 293–300. [CrossRef]
16. Ross, L.; Sottolichio, A.; Maury, T.; Lesourd, S. Intratidal and Subtidal Circulation in a Tropical Estuary during Wet Season: The Maroni, French Guiana. *Mar. Sci. Eng.* **2019**, *7*, 433. [CrossRef]
17. Wright, L.D. Dispersal and deposition of river sediments in coastal seas: Models from Asia and the tropics. *Neth. J. Sea Res.* **1989**, *23*, 493–500. [CrossRef]
18. Shimozono, T.; Tajima, Y.; Akamatsu, S.; Matsuba, Y.; Kawasaki, A. Large-Scale Channel Migration in the Sittang River Estuary. *Sci. Rep.* **2019**, *9*, 1–9. [CrossRef] [PubMed]
19. Anthony, E.J. The muddy tropical coast of West Africa from Sierra Leone to Guinea- Bissau: Geological heritage, geomorphology and sediment dynamics. *Afr. Geosci. Rev.* **2006**, *13*, 227–237.
20. Martinez, J.M.; Guyot, J.L.; Filizola, N.; Sondag, F. Increase in suspended sediment discharge of the Amazon River assessed by monitoring network and satellite data. *Catena* **2009**, *79*, 257–264. [CrossRef]
21. Wittmann, H.; von Blanckenburg, F.; Maurice, L.; Guyot, J.L.; Filizola, N.; Kubik, P.W. Sediment production and delivery in the Amazon River basin quantified by in situ- produced cosmogenic nuclides and recent river loads. *GSA Bull.* **2010**, *123*, 934–950. [CrossRef]
22. Anthony, E.J.; Gardel, A.; Gratiot, N.; Proisy, C.; Allison, M.A.; Dolique, F.; Fromard, F. The Amazon-influenced muddy coast of South America: A review of mud-bank-shoreline interactions. *Earth Sci. Rev.* **2010**, *103*, 99–121. [CrossRef]
23. Anthony, E.J.; Gardel, A.; Gratiot, N. Fluvial sediment supply, mud banks, cheniers and the morphodynamics of the coast of South America between the Amazon and Orinoco river mouths. *Geol. Soc. Lond. Spec. Publ.* **2014**, *388*, 533–560. [CrossRef]
24. Wells, J.T.; Coleman, J.M. Longshore Transport of Mud by Waves: Northeastern Coast of South America. *Geol. En Mijnb.* **1978**, *57*, 353–359.
25. Rodriguez, H.N.; Mehta, A.J. Modelling muddy coast response to waves. *J. Coast. Res.* **2001**, 137–148.
26. Chevalier, C.; Baklouti, M.; Ramamonjiarisoa, A. Modeling the influence of wind and rivers on current, salinity and temperature over the French Guiana continental shelf during the rainy season. *J. Coast. Res.* **2004**, *20*, 1183–1197. [CrossRef]
27. Gratiot, N.; Gardel, A.; Anthony, E.J. Trade-wind waves and mud dynamics on the French Guiana coast, South America: Input from ERA-40 wave data and field investigations. *Mar. Geol.* **2007**, *236*, 15–26. [CrossRef]
28. Chevalier, C.; Froidefond, J.M.; Devenon, J.L. Numerical analysis of the combined action of littoral current, tide and waves on the suspended mud transport and on turbid plumes around French Guiana mudbanks. *Cont. Shelf Res.* **2008**, *28*, 545–560. [CrossRef]
29. Abascal-Zorrilla, N.; Vantrepotte, V.; Gensac, E.; Huybrechts, N.; Gardel, A. The Advantages of Landsat 8-OLI-Derived Suspended Particulate Matter Maps for Monitoring the Subtidal Extension of Amazonian Coastal Mud. *Remote Sens.* **2018**, *10*, 1733. [CrossRef]
30. Augustinus, P.G.E.F. *Morphological Considerations in Relation to Channel Deepening in the Suriname River*; Sunecon: Paramaribo, Suriname, 2016.
31. Anthony, E.J.; Gardel, A.; Proisy, C.; Fromard, F.; Gensac, E.; Peron, C.; Walcker, R.; Lesourd, S. The role of fluvial sediment supply and river-mouth hydrology in the dynamics of the muddy, Amazon-dominated Amapá-Guianas coast, South America: A three-point research agenda. *J. South Am. Earth Sci.* **2013**, *44*, 18–24. [CrossRef]
32. Todd, T. Dynamic Diversion: Influence of Longshore Current-Tidal Flow Interaction on Chenier and Barrier Island Plains. *SEPM J. Sediment. Res.* **1968**, *38*, 734–746. [CrossRef]
33. Jouanneau, J.M.; Pujos, M. Variations annuelles des concentrations en matières en suspension et estimations des débits solides des fleuves Maroni et Mahury (Guyane Française). *Geol. De La Fr.* **1988**, *2*, 163–169.
34. Rousseau, T.C.C.; Roddaz, M.; Moquet, J.S.; Handt Delgado, H.; Calves, G.; Bayon, G. Controls on the geochemistry of suspended sediments from large tropical South American rivers (Amazon, Orinoco and Maroni). *Chem. Geol.* **2019**, *522*, 38–54. [CrossRef]
35. Do, A.T.K.; Huybrechts, N.; Sottolichio, A.; Gardel, A. Modeling and Quantification of Patterns of Salinity, Mixing and Subtidal Flow in the Maroni Estuary. In *International Conference on Asian and Pacific Coasts*; Springer: Singapore, 2019. [CrossRef]

36. Jolivet, M.; Anthony, E.J.; Gardel, A.; Brunier, G. Multi-Decadal to Short-Term Beach and Shoreline Mobility in a Complex River-Mouth Environment Affected by Mud From the Amazon. *Front. Earth Sci.* **2019**, *7*, 1–17. [CrossRef]
37. Froidefond, J.M.; Lahet, F.; Hu, C.; Doxaran, D.; Guiral, D.; Prost, M.T.; Ternon, J.F. Mudflats and mud suspension observed from satellite data in French Guiana. *Mar. Geol.* **2004**, *208*, 153–168. [CrossRef]
38. Gardel, A.; Gratiot, N. A Satellite Image–Based Method for Estimating Rates of Mud Bank Migration, French Guiana, South America. *J. Coast. Res.* **2005**, *214*, 720–728. [CrossRef]
39. Eisma, D.; Augustinus, P.G.E.F.; Alexander, C. Recent and subrecent changes in the dispersal of amazon mud. *Neth. J. Sea Res.* **1991**, *28*, 181–192. [CrossRef]
40. Curtin, T.B. Physical observations in the plume region of the Amazon River during peak discharge-II. Water masses. *Cont. Shelf Res.* **1986**, *6*, 53–71. [CrossRef]
41. Gibbs, R.J. Sites of river-derived sedimentation in the ocean. *Geology* **1981**, *9*, 77–80. [CrossRef]
42. Oliveira, C.J.M.; Clavier, J. Variations spatio-temporelles des matieres en suspension dans I'estuaire du Sinnamary, Guyane française: Influence du barrage hydroélectrique de Petit Saut. *Rev. Bras. Oceanogr.* **2000**, *48*, 29–39. [CrossRef]
43. Sondag, F.; Guyot, J.L.; Moquet, J.S.; Laraque, A.; Adele, G.; Cochonneau, G.; Doudou, J.C.; Lagane, C.; Vauchel, P. Suspended sediment and dissolved load budgets of two Amazonian rivers from the Guiana Shield: Maroni River at LangaTabiki and Oyapock River at SautMaripa (French Guiana). *Hydrol. Process. Int. J.* **2010**, *24*, 1433–1445. [CrossRef]
44. Gallay, M.; Martinez, J.M.; Mora, A.; Laraque, A.; Claude, J. Impact of land degradation from mining activities on the sediment fluxes in two large rivers of French Guiana. *Land Degrad. Dev.* **2018**, 4323–4336. [CrossRef]
45. Abascal-Zorrilla, N.; Vantrepotte, V.; Ngoc, D.D.; Huybrechts, N.; Gardel, A. Automated SWIR based empirical sun glint correction of Landsat 8-OLI data over coastal turbid water. *Opt. Express* **2019**, *27*, 294–318. [CrossRef] [PubMed]
46. Ngoc, D.D.; Loisel, H.; Jamet, C.; Vantrepotte, V.; Duforêt-Gaurier, L.; Minh, C.D.; Mangin, A. Coastal and inland water pixels extraction algorithm (WiPE) from spectral shape analysis and HSV transformation applied to Landsat 8 OLI and Sentinel-2 MSI. *Remote Sens. Environ.* **2019**, *223*, 208–228. [CrossRef]
47. Han, B.; Loisel, H.; Vantrepotte, V.; Mériaux, X.; Bryère, P.; Ouillon, S.; Dessailly, D.; Xing, Q.; Zhu, J. Development of a Semi-Analytical Algorithm for the Retrieval of Suspended Particulate Matter from Remote Sensing over Clear to Very Turbid Waters. *Remote Sens.* **2016**, *8*, 211. [CrossRef]
48. Uncles, R.J.; Stephens, J.A.; Law, D.J. Turbidity maximum in the macrotidal, highly turbid Humber Estuary, UK: Flocs, fluid mud, stationary suspensions and tidal bores. *Estuar. Coast. Shelf Sci.* **2006**, *67*, 30–52. [CrossRef]
49. Tolman, H.L. *User Maual and System Documentation of WAVEWATCH-III Version 1.15 NOAA/NWS/NCEP/OMB*; Technical Note; NOAA, NWS, NCEP: US Department of Commerce, College Park, MD, USA, 1997; Volume 151, p. 97.
50. Tolman, H.L. *User Maual and System Documentation of WAVEWATCH-III Version 1.18. NOAA/NWS/NCEP/OMB*; Technical Note; NOAA, NWS, NCEP: US Department of Commerce, College Park, MD, USA, 1999; Volume 166, p. 110.
51. Tolman, H.L. *User Maual and System Documentation of WAVEWATCH-III Version 1.18. NOAA/NWS/NCEP/MMAB*; Technical Note; NOAA, NWS, NCEP: US Department of Commerce, College Park, MD, USA, 2009; Volume 279, p. 194.
52. Geyer, W.R.; Woodruff, J.D.; Traykovski, P. Sediment transport and trapping in the Hudson River estuary. *Estuaries* **2001**, *24*, 670–679. [CrossRef]
53. Toorman, E.A.; Anthony, E.; Augustinus, P.G.E.F.; Gardel, A.; Gratiot, N.; Homenauth, O.; Huybrechts, N.; Monbaliu, J. Interaction of Mangroves, Coastal Hydrodynamics, and Morphodynamics Along the Coastal Fringes of the Guianas. *Threat. Mangrove For.* **2018**, *20*, 429–473.
54. Scully, M.E.; Friedrichs, C.T. The influence of asymmetries in overlying stratification on near-bed turbulence and sediment suspension in a partially mixed estuary. *Ocean Dyn.* **2003**, *53*, 208–219. [CrossRef]
55. Schubel, J.R. Turbidity maximum of the Northern Chesapeake Bay. *Science* **1968**, *161*, 1013–1015. [CrossRef]
56. Postma, H. Sediment Processes in Estuaries: Some Evaluating Remarks. In *Physical Processes in Estuaries*; Dronkers, J., Van Leussen, W., Eds.; Springer: Berlin/Heidelberg, Germany, 1988; pp. 547–551.

57. Uncles, R.J.; Stephens, J.A.; Smith, R.E. The dependence of estuarine turbidity on tidal intrusion length, tidal range and residence time. *Cont. Shelf Res.* **2002**, *22*, 1835–1856. [CrossRef]
58. Berthois, L.; Hoorelbeck, J. *Etude dynamique de la sédimentation auxs trois cours d'eau de la Guyane française: La rivière Mahury, la rivière de Cayenne, et le fleuve Maroni*; Mémoires ORSTOM: Paris, France, 1968.
59. Asp, N.E.; Gomes, V.J.C.; Schettini, C.A.F.; Souza-Filho, P.W.M.; Siegle, E.; Ogston, A.S.; Nittrouer, C.A.; Silva, J.N.S.; Nascimento, W.R.; Souza, S.R.; et al. Sediment dynamics of a tropical tide-dominated estuary: Turbidity maximum, mangroves and the role of the Amazon River sediment load. *Estuar. Coast. Shelf Sci.* **2018**, *214*, 10–24. [CrossRef]
60. Anthony, E.J.; Dolique, F.; Gardel, A.; Gratiot, N.; Proisy, C.; Polidori, L. Nearshore intertidal topography and topographic-forcing mechanisms of an Amazon-derived mud bank in French Guiana. *Cont. Shelf Res.* **2008**, *28*, 813–822. [CrossRef]
61. Orseau, S.; Abascal-Zorrilla, N.; Huybrechts, N.; Lesourd, S.; Gardel, A. Decadal-Scale Morphological Evolution of a Muddy Open Coast. *Mar. Geol.* **2020**, *420*, 106048. [CrossRef]
62. Migniot, C. Etude des propriétés physiques de différents sédiments très fins et de leur comportement sous des actions hydrodynamiques. *La Houille Blanch.* **1968**, *7*, 591–620. [CrossRef]
63. NEDECO. *Suriname Transportation Study. Report on Hydraulic Investigation*; Delft Hydraulics: The Hague, The Netherlands, 1968; Volume 293.
64. Allison, M.A.; Lee, M.T. Sediment exchange between Amazon mudbanks and shore-fringing mangroves in French Guiana. *Mar. Geol.* **2004**, *208*, 169–190. [CrossRef]
65. Vantrepotte, V.; Gensac, E.; Loisel, H.; Gardel, A.; Dessailly, D.; Mériaux, X. Satellite assessment of the coupling between in water suspended particulate matter and mud banks dynamics over the French Guiana coastal domain. *J. S. Am. Earth Sci.* **2013**, *44*, 25–34. [CrossRef]
66. Walcker, R.; Gratiot, N.; Anthony, E.J. Remote Sensing-based Monitoring of the Muddy Mangrove Coastline of French Guiana. *L. Surf. Remote Sens. Urban. Coast. Areas* **2016**, 297–320. [CrossRef]